The Life Cycle of Spontaneously Generated Internal Waves

CALLUM J. SHAKESPEARE AND ANDREW MCC. HOGG

*Research School of Earth Sciences, and Australian Research Council Centre of Excellence in Climate System Science,
Australian National University, Canberra, Australian Capital Territory, Australia*

ABSTRACT

Recent numerical modeling studies have suggested significant spontaneous internal wave generation near the ocean surface and energy transfers to and from these waves in the ocean interior. Spontaneous generation is the emission of waves by unbalanced, large Rossby number flows in the absence of direct forcing. Here, the authors' previous work is extended to investigate where and how these waves exchange energy with the nonwave (mean) flow. A novel double-filtering technique is adopted to separate first the wave and nonwave fields, then the individual upward- and downward-propagating wave fields, and thereby identify the pathways of energy transfer. These energy transfers are dominated by the interaction of the waves with the vertical shear in the mean flow. Spontaneously generated waves are found to be oriented such that the downward-propagating wave is amplified by the mean shear. The internal waves propagate through the entire model depth while dissipating energy and reflect back upward. The now-upward-propagating waves have the opposite sign interaction with the mean shear and decay, losing most of their energy to the nonwave flow in the upper 500 m. Overall, in the simulations described here, approximately 30% of the wave energy is dissipated, and 70% is returned to the mean flow. The apparent preferential orientation of spontaneous generation suggests a potentially unique role for these waves in the ocean energy budget in uniformly drawing net energy from mean flow in the upper-ocean interior and transporting it to depth.

1. Introduction

The generation of internal waves is a vital mechanism by which energy can be fluxed downscale and ultimately support mixing in the deep ocean (Wunsch and Ferrari 2004). The major sources of internal waves in the ocean are tidal flows over rough bottom topography and high-frequency winds blowing over the ocean surface (Munk 1981). Geostrophic flows interacting with bottom topography are also able to generate internal lee waves (Nikurashin and Ferrari 2011). In addition, internal waves can be generated through forced imbalances triggering fluid dynamical instabilities, which then radiate waves (e.g., Plougonven and Zeitlin 2009; Ribstein et al. 2014; Grisouard et al. 2016). Waves are also generated "spontaneously" near the ocean surface without any external forcing, imbalance, or topographic interactions in situations where the large-scale balanced flow breaks down, often associated with frontogenesis (e.g., Nagai et al. 2015; Shakespeare and Taylor 2016; Shakespeare and Hogg 2017a). Here, we focus on such

spontaneous generation and extend the analysis of Shakespeare and Hogg (2017a) to resolve the life cycle of these internal waves.

In addition to the spontaneous generation of internal waves, energy can be transferred to preexisting waves from balanced flows or from balanced flows to the wave field. Such mean-to-wave (MTW) exchanges play a dominant role in the wave energy budget of Shakespeare and Hogg (2017a) and in the present work. Earlier work investigated the interactions of a linear wave field with various background flows (e.g., Eliassen and Palm 1961; Jones 1967). In their seminal paper, Eliassen and Palm (1961) showed that internal waves (in their case, steady lee waves) will gain (lose) energy from a shear flow that increases (decreases) with height above topography but have unchanged pseudomomentum flux. This interaction of internal waves with the mean shear is identified as the dominant mean-to-wave energy transfer in our simulations and is discussed in detail in section 4.

The crucial element of the analysis of Shakespeare and Hogg (2017a) [and, previously, Nagai et al. (2015)] is the application of a Lagrangian filter to separate the "wave" and "nonwave parts" of the flow. Consistent

Corresponding author: Callum J. Shakespeare, callum.shakespeare@anu.edu.au

with previous work, here we will use the terms "non-wave" and "mean" interchangeably to describe all flow that is not internal waves, including turbulent flow such as jets and eddies. The Lagrangian filter is based on the definition of an internal wave as a motion of Lagrangian frequency (frequency following the local flow) exceeding the inertial frequency (e.g., Polzin and Lvov 2011) and addresses the issue of significant Doppler shifting of the wave frequency by the nonwave flow, which is common in regions of spontaneous generation where flow velocities are large (e.g., Shakespeare and Taylor 2016). The robust identification of the wave field permitted Shakespeare and Hogg (2017a) to determine the fluxes between the wave and the nonwave flow and thereby form a balanced energy budget for the internal wave field. Shakespeare and Hogg (2017a) reported very large fluxes of energy (up to $90\,\mathrm{mW\,m^{-2}}$) into the wave field near fronts and filaments in the surface 50 m of their model. However, much of this generation was compensated by neighboring large fluxes of energy in the reverse direction, from the waves to the nonwave flow. It was not clear from their results the pathway of the wave energy between the sources and neighboring sinks of energy. Here, we are able to extend the analysis of the simulated wave field to resolve this energy pathway.

Our methodology is to apply a secondary filter to the (already Lagrangian filtered) wave field to separate upward- and downward-propagating waves. We can then independently calculate the energy exchanges of up- and downgoing waves with the mean flow. We will show that the energy flux is almost entirely from the mean flow to downgoing waves and from upgoing waves back to the mean flow. That is, downgoing waves are spontaneously generated and then amplified by the mean flow and reflect off the bottom, and the resultant upgoing waves lose energy back to the mean flow. Furthermore, we can track the dissipation of wave energy of the down- and upgoing waves over the ocean depth, allowing us to fully elucidate the life cycle of the spontaneously generated internal waves. We perform this analysis for three different simulations with different bottom boundaries, including flat and rough topographies and the case with a viscous sponge layer studied in Shakespeare and Hogg (2017a). The life cycle of the internal waves is similar in all three cases, but with important differences arising due to differing wave reflections and dissipation near the ocean bottom.

The paper is set out as follows. In section 2, we describe the three model configurations and the filtering methodology. In section 3b, we formulate balanced energy budgets for the three simulations and identify the sources and sinks of down- and upgoing wave energy. We then use these results (section 3c) to describe the

complete life cycle of the internal waves, from spontaneous generation to eventual reabsorption or dissipation. The spatial distribution of the energy sources and sinks (section 3d) motivates a detailed discussion (section 4) of the mechanism of energy transfer between the wave and nonwave flow. Last, in section 5, we reflect on the implications of our results for the role and significance of spontaneously generated waves in the ocean energy budget.

2. Methods

a. Model configurations

The basic model configuration is identical to that of Shakespeare and Hogg (2017a). We use the Massachusetts Institute of Technology general circulation model (MITgcm; Marshall et al. 1997) to simulate the hydrostatic primitive equations in a 500-km square, zonally reentrant, f-plane channel at 200-m horizontal resolution. The vertical grid consists of 200 points with grid spacing of 1.5 m at the surface, increasing to 40 m at middepth and reducing to 20 m in the deepest 1 km of the domain. All simulations are forced by "sponges" of 30-km width just inside the northern and southern boundaries, where densities (temperatures; salinity is constant) are restored to specified profiles on a 10-day time scale. No surface wind stresses or surface buoyancy fluxes are imposed. The vertical grid and relaxation profiles are shown in Shakespeare and Hogg (2017a, see Fig. 1 therein). Subgrid turbulence is parameterized via Laplacian diffusion and viscosity. In the absence of boundary fluxes, there is no requirement for significant vertical viscosity or diffusivity, and these parameters are set to a negligible value everywhere ($A_v = \kappa_v = 10^{-6}\,\mathrm{m^2\,s^{-1}}$). Guided by the results of Shakespeare and Hogg (2017b), in order to maintain stability in the model interior with negligible spurious wave decay, we apply a uniform horizontal diffusivity of $\kappa_h = 0.1\,\mathrm{m^2\,s^{-1}}$ (constant over the entire domain). Horizontal viscosity is employed near boundaries to maintain model stability, as described below.

Here, we consider three different simulations: (A) flat bottom at 3700-m depth, (B) rough bottom with a mean depth of 3700 m, and (C) flat bottom at 3700 m with a viscous sponge below 2500 m (the simulation described in Shakespeare and Hogg 2017a). Snapshots of the surface vorticity from simulations (A) and (B) are shown in Figs. 1a and 1b, respectively—both simulations have an active submesoscale, but the large-scale flow is significantly modified by the presence of topography. The topography in simulation (B) is shown in Fig. 1e and consists of a smooth Gaussian hill 800 m high, overlaid with small-scale random roughness on wavelengths from 10 to 100 km and root-mean-square height of 300 m.
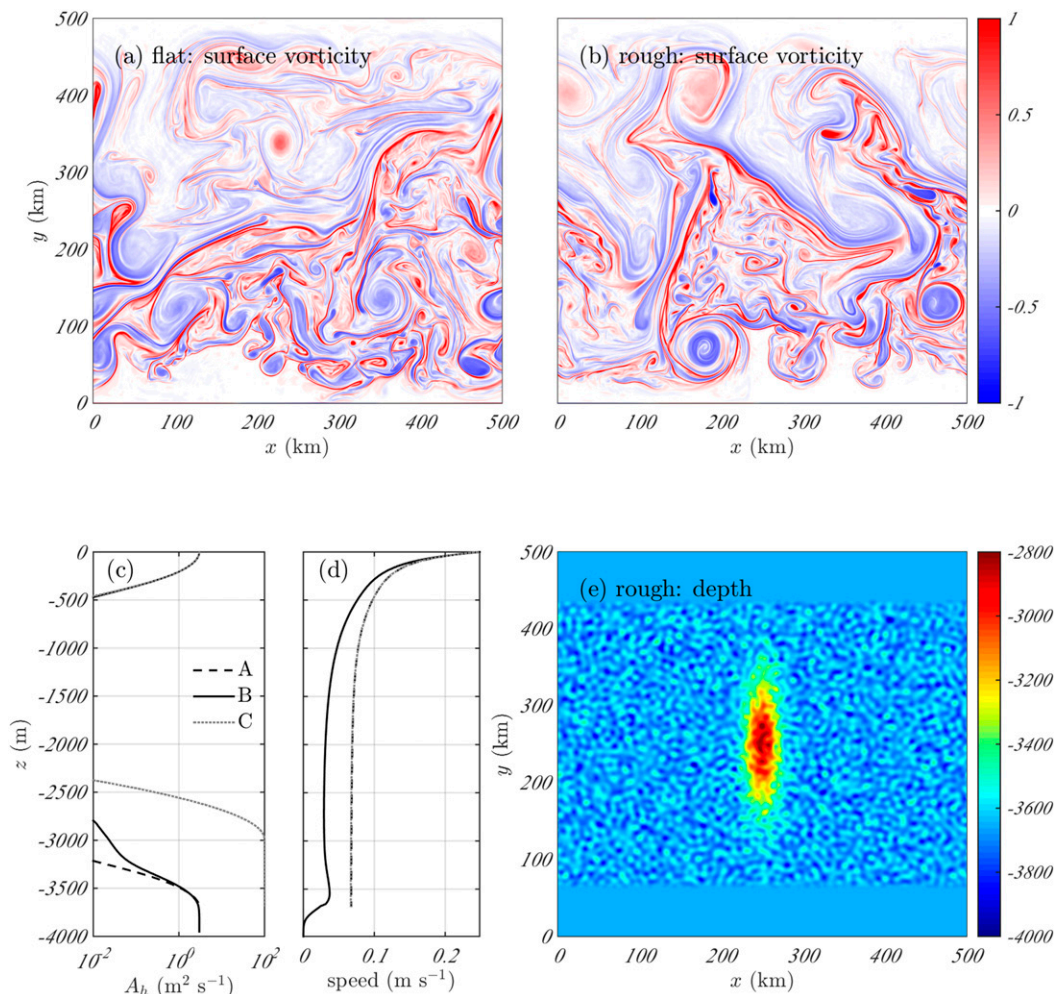
FIG. 1. Configuration and model state of the three simulations considered here. Snapshot of surface vorticity $(\partial_x v - \partial_y u)/f$ for the (a) flat case and (b) rough case. (c) Mean horizontal viscosity with depth in the three simulations: case (A): flat; case (B): rough; and case (C): flat sponge. (d) Mean flow speed with depth in the three simulations. (e) Model depth in the rough case.

The combination of the large smooth hill (seamount) and the small-scale roughness has been chosen to simultaneously modify both the momentum balance of the large-scale flow and the reflections of internal waves, compared with the flat-bottomed simulations. The topography is flat in the temperature-restoring sponge regions at the northern and southern edges of the domain. In simulations (A) and (B), the horizontal viscosity is set to $A_h = 3 \, \text{m}^2 \, \text{s}^{-1}$ near the surface and bottom and decays with a 200-m e-folding scale to a negligible interior value of $10^{-6} \, \text{m}^2 \, \text{s}^{-1}$. In simulation (C), the viscosity is identical to the other simulations near the surface but increases to $100 \, \text{m}^2 \, \text{s}^{-1}$ in the sponge below 2500 m. The mean viscosity as a function of depth in each case is shown in Fig. 1c. The mean flow speed with depth is shown in Fig. 1d for reference.

The three configurations have been carefully chosen to isolate the process of spontaneous generation of internal waves. The two flat-bottomed cases, (A) and (C), have no other possible means of wave generation. The difference between these two cases is expected to be the amount of reflection versus dissipation near the bottom boundary. The rough bottom case (B) has the potential for lee wave generation as geostrophic currents and eddies flow over the bottom topography. However, the scales of the topography have been chosen such that the minimum wavelength is 10 km (or maximum wavenumber is $k = 2\pi/10^4$), and, hence, bottom flow speeds must exceed $U = f/k = 0.2 \, \text{m} \, \text{s}^{-1}$ for linear lee wave generation (Bell 1975). Bottom flow speeds are typically half this value or less; thus, negligible linear lee wave generation is observed in

the model, although the topography still gives rise to a small but nonnegligible net transfer of energy to the wave field (to be shown later). Such energy fluxes may occur via a topography-induced amplification of preexisting waves, or else generation of new waves via flow instabilities or nonlinear dynamics near topography.

b. Analysis methodology

Here, we describe the formulation of an energy budget for an internal wave field to be applied in each of our simulations in section 3b. Following the methodology of Shakespeare and Hogg (2017a), we use a Lagrangian filtering technique to separate the internal wave field from the remainder of the nonwave flow. The wave field is defined as Lagrangian frequencies exceeding the inertial frequency f, analyzed for hourly data over a 1-week period. For the details of this method, the reader is referred to the appendix. This filtering method leads to a clear spatiotemporal scale separation between the wave and nonwave (mean) flow fields, such that the time and horizontal space average (denoted $\langle \rangle$) of a wave field (denoted $\tilde{\phi}$) and a nonwave field (denoted $\overline{\phi}$) is zero. With this result, it is possible to formulate a closed energy budget for the wave field. Following Shakespeare and Hogg (2017a), the steady-state energy budget for the wave field (in the absence of external forcing) may be derived as

$$0 = \left\langle \mathscr{B} + \int_{-H}^{0} \left(-D + \mathscr{F}_{\mathrm{MTW}} \right) dz \right\rangle, \qquad (1)$$

where $\mathscr{B}$ is the bottom flux, D is the sign-definite dissipation of wave energy either viscously or through mixing, and $\mathscr{F}_{\mathrm{MTW}}$ is the energy flux from the mean to the wave field. Here we use standard Cartesian coordinates where $\tilde{\mathbf{u}} = (u, v, w)$ is the velocity in the (x, y, z) directions, p is the pressure, and b is the buoyancy. The bottom flux is defined as

$$\mathscr{B} = \int_{S} \tilde{\mathbf{u}} \tilde{p} \cdot \hat{\mathbf{n}} \, dS, \qquad (2)$$

evaluated in the cell above topography, where $\hat{\mathbf{n}}$ is a unit normal to the surface S, and includes bottom drag and any topographic wave–mean interactions, including wave generation or amplification. The dissipation is defined as

$$D = \underbrace{A_h |\nabla_h \tilde{\mathbf{u}}_h|^2 + A_v \left| \frac{\partial \tilde{\mathbf{u}}_h}{\partial z} \right|^2}_{\text{viscous dissipation}} + \underbrace{\frac{\kappa_h}{N^2} |\nabla_h \tilde{b}|^2 + \frac{\kappa_v}{N^2} \left(\frac{\partial \tilde{b}}{\partial z} \right)^2}_{\text{irreversible mixing}}, \qquad (3)$$

where subscript h denotes the horizontal part, subscript v the vertical part, κ the diffusivity, A the viscosity, and $N^2 = \langle \partial_z \overline{b} \rangle$. Last, the energy transfer from the mean to the wave field is

$$\mathscr{F}_{\mathrm{MTW}} = \underbrace{-\tilde{w}\tilde{\mathbf{u}}_h \cdot \frac{\partial \overline{\mathbf{u}}_h}{\partial z}}_{\text{vertical shear}} \underbrace{-\tilde{b}\tilde{\mathbf{u}}_h \cdot \frac{\nabla_h \overline{b}}{N^2}}_{\text{potential}}$$

$$\underbrace{-\tilde{u}^2 \frac{\partial \overline{u}}{\partial x} - \tilde{v}^2 \frac{\partial \overline{v}}{\partial y} - \tilde{u}\tilde{v} \left(\frac{\partial \overline{u}}{\partial y} + \frac{\partial \overline{v}}{\partial x} \right)}_{\text{horizontal shear}}. \qquad (4)$$

The mean-to-wave conversion is, thus, composed of three terms involving the interaction of the wave field with different properties of the mean flow: (i) mean vertical shear, (ii) mean horizontal buoyancy gradients (involving potential energy exchange), and (iii) mean horizontal shear.

It is insightful to nondimensionalize the mean-to-wave flux expression (4). We assume that the mean flow has a horizontal length scale L, vertical length scale H, speed U, and $|\nabla_h b| \sim fU/H$. We assume that the wave flow has frequency ω, vertical wavenumber m, and horizontal wavenumber k, such that $\tilde{u} \sim u_0$, $\tilde{w} \sim (k/m)u_0$, and $\tilde{b} \sim N^2 \tilde{w}/\omega$. With these scales, Eq. (4) may be written as (all fields on the right-hand side assumed nondimensional and of order 1)

$$\mathscr{F}_{\mathrm{MTW}} = fu_0^2 \left\{ \begin{array}{l} \dfrac{\sqrt{\omega^2 - f^2}}{f} \mathrm{Fr} \left(-\tilde{w}\tilde{\mathbf{u}}_h \cdot \dfrac{\partial \overline{\mathbf{u}}_h}{\partial z} - \tilde{b}\tilde{\mathbf{u}}_h \cdot \dfrac{\nabla_h \overline{b}}{N^2} \right) \\[3mm] + \mathrm{Ro} \left[-\tilde{u}^2 \dfrac{\partial \overline{u}}{\partial x} - \tilde{v}^2 \dfrac{\partial \overline{v}}{\partial y} - \tilde{u}\tilde{v} \left(\dfrac{\partial \overline{u}}{\partial y} + \dfrac{\partial \overline{v}}{\partial x} \right) \right] \end{array} \right\},$$

$$(5)$$

where we have used the dispersion relation for linear hydrostatic internal waves $\omega = \sqrt{f^2 + N^2 k^2/m^2}$, $\mathrm{Ro} = U/(fL)$ is the Rossby number, and $\mathrm{Fr} = U/(NH)$ is the Froude number. This scaling analysis indicates that (i) the horizontal shear terms scale with Rossby number and will, therefore, be largest near boundaries; (ii) the vertical shear and potential terms will vanish for near-inertial waves; and (iii) for sufficiently superinertial waves, the vertical shear and potential terms scale with the Froude number and are independent of Rossby number. We will test these scalings below.

Here, we extend the energy budget analysis of Shakespeare and Hogg (2017a): we filter the wave field into upward- and downward-propagating components and separate the dissipation (3) and mean-to-wave energy flux (4) into that associated with the upward and downward waves. The up–down filtering is carried out based on vertical phase speed as follows. First, the wave field is Fourier transformed in time $(t \mapsto \omega)$ and vertical position $(z \mapsto m)$ at each horizontal location. Signals with frequency $\omega > 0$ and wavenumber $m > 0$ or with

$\omega < 0$ and $m < 0$ may be identified as having vertical phase speeds $c_p = -\omega/m < 0$ and, consequently, vertical group speeds greater than zero (upward propagating). The remaining downward-propagating part of the signal is masked, and the field is inverse Fourier transformed to give the upward-propagating wave field in (x, y, z, t) space. The dissipation and mean-to-wave fluxes can then be independently computed for the upward- and downward-traveling waves.[1]

3. Results

a. Frequency spectra

Figure 2 displays frequency spectra of the kinetic energy averaged along Lagrangian parcel trajectories for each of the three simulations: (A) flat, (B) rough, and (C) flat sponge. In each case, there is a clear spatio-temporal scale separation between nonwave energy at low frequencies and wave energy at frequencies greater than or equal to the inertial (as required for the Lagrangian filtering method to be applicable). The spectrum of the wave field is comparable in all three simulations, with energy strongly concentrated at near-inertial frequencies (approximately 90% of the energy is at frequencies less than $1.3f$).

b. Global energy budgets

Figure 3 displays the domain-integrated wave energy budgets for the three simulations: (A) flat (red), (B) rough (green), and (C) flat sponge (blue). Despite the differences in bottom boundaries, all simulations show similar behavior. Energy is transferred into the downgoing wave field (dark shades) from the mean flow and returned to the mean flow from the upgoing wave field (light shades). Some wave energy is lost to dissipation from both the up- and downgoing wave fields. The bottom flux terms are small and negative in the flat bottom cases and positive for the rough bottom case. The residuals (shown as gray bars on the top row of Fig. 3) are negligible in each case—that is, the wave energy budget in each simulation is essentially balanced. The dominant balance is between energy input to the downgoing wave field—which includes both spontaneous
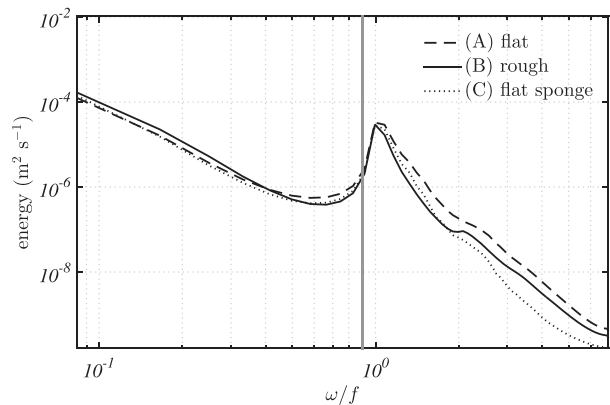
---

[1] In the general case, there are additional nonlinear wave–wave interaction terms (e.g., Müller et al. 1986) that can transfer energy between the upward- and downward-propagating waves, but these are found to be negligible in the present simulations and are not discussed here. However, nonlinear interactions between waves in the same vertical direction may be significant but occur entirely within the downward or upward wave fields and so are not identifiable in the present energetics analysis.

FIG. 2. The kinetic energy spectrum ($m^2 s^{-1}$) averaged along particle trajectories as a function of Lagrangian frequency ω (normalized by f). Internal waves are identified as signals to the right of the gray line located at $0.9f$; see Shakespeare and Hogg (2017a).

generation of waves and the amplification of those waves—and energy loss from the upgoing wave field. This balance implies a transfer of downgoing energy to upgoing energy, for example, via the reflection of downgoing waves off the bottom of the model ocean.

The vertical structure of the energy source and sink terms for up- and downgoing wave energy is shown in Fig. 4 for each of the simulations. The sum of the sources and sinks at a given depth is shown in black. The surface 30 to 50 m is dominated by very large energy fluxes into the downgoing wave field. As described in Shakespeare and Hogg (2017a), these fluxes are associated with spontaneous generation at fronts and filaments undergoing active frontogenesis. Below this surface generation region is a layer from 200- to 500-m depth that is dominated by the dissipation of both down- and upgoing waves (in similar amounts). Below this, from 500- to 2500-m depth, the energy budget is again dominated by the mean-to-wave terms. The downgoing waves are amplified by the mean flow, and the upgoing waves decay. In all simulations, the amplification of the downgoing waves is larger, but by differing amounts. Below 2500-m depth, the details of the energy budget vary depending on the different bottom boundary in each case. The flat bottom simulation (A) has sizeable dissipation of both up- and downgoing waves near the smooth bottom boundary. The flat sponge simulation (C) has very large dissipation of downgoing waves at the upper edge of the sponge (~2700 m). The rough bottom simulation (B) has a mix of processes operating, including energy gain from topographic interactions (bottom flux; gray line), dissipation, and mean-to-wave conversions. The mean-to-wave conversions flip signs in this region, with downgoing waves losing energy and
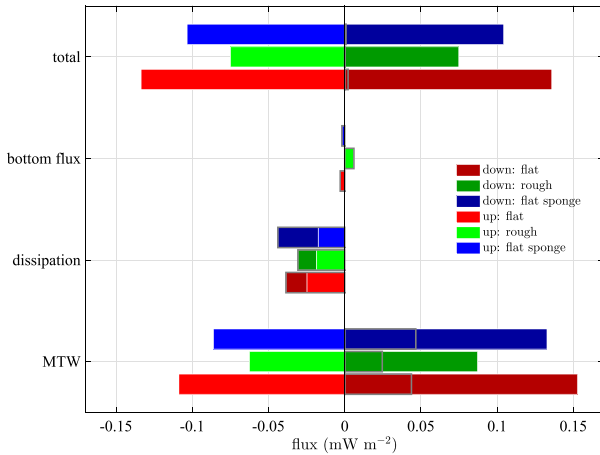
FIG. 3. Domain-averaged wave energy budget for the three simulations: flat (A; red), rough (B; green), and flat sponge (C; blue). Energy fluxes associated with upgoing waves are rendered in a lighter shade, and those associated with downgoing waves are rendered in a darker shade. The net energy flux for each process (up plus down) is shown as a gray box. The dominant balance is between energy going into the downgoing waves from the mean flow (MTW > 0) and energy being reabsorbed by the mean flow from the upgoing waves (MTW < 0), with around 30% dissipating.

upgoing waves gaining energy, owing to the reversal of the mean vertical shear near topography (see Fig. 1d).

c. The internal wave life cycle

The vertical structure of the energy sources and sinks shown in Fig. 4 motivates the identification of three regions, each with distinct behavior: the upper ocean,

above 500 m; the interior, between 500 and 2500 m; and the deep, below 2500 m. The upper-ocean region is responsible for the generation and amplification of downgoing waves, the absorption of upgoing waves, and the dissipation of both up- and downgoing waves. The interior region exhibits a balance between amplification of downgoing waves and decay of upgoing waves. The deep region behavior varies and is determined by the bottom boundary (flat, rough, or sponge).

Figure 5 displays a schematic wave life cycle for each of the simulations, with the sources and sinks of wave energy identified as sums over the surface, interior, and deep regions. The magnitudes are normalized in each simulation by setting the generation and amplification of downgoing wave energy in the surface region to 100 units, allowing for comparison of the percentage energy gains and losses. The wave path shown applies for an internal wave generated spontaneously at the surface, which undergoes a single reflection off the ocean bottom and propagates back into the upper ocean, where it completely loses its remaining energy to the mean flow. However, this is only a schematic picture: there is the possibility of additional reflections off the surface or bottom.

We first compare the wave life cycle in the flat bottom simulations: (A) and (C). The mean flow (e.g., Fig. 1d) in these cases is nearly identical, with differences in the wave energy budget arising due to the presence of the deep viscous sponge in (C) that absorbs additional, mostly downgoing, wave energy. Of the 100 units of generation/amplification in the top 500 m, both (A) and
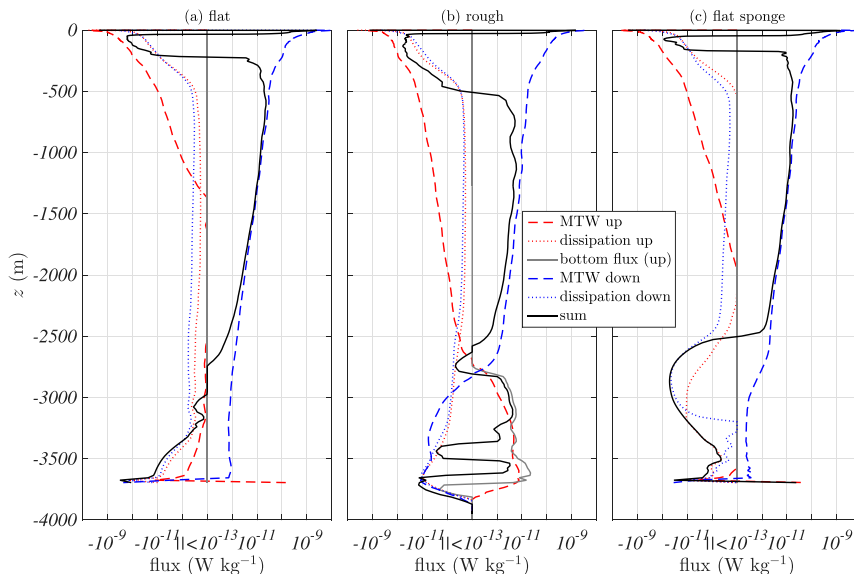

FIG. 4. Vertical profiles of the sources and sinks of wave energy (W kg⁻¹) for the three simulations: (a) flat (case A), (b) rough (case B), and (c) flat sponge (case C). The sum of all sources and sinks at a given depth is shown in black.
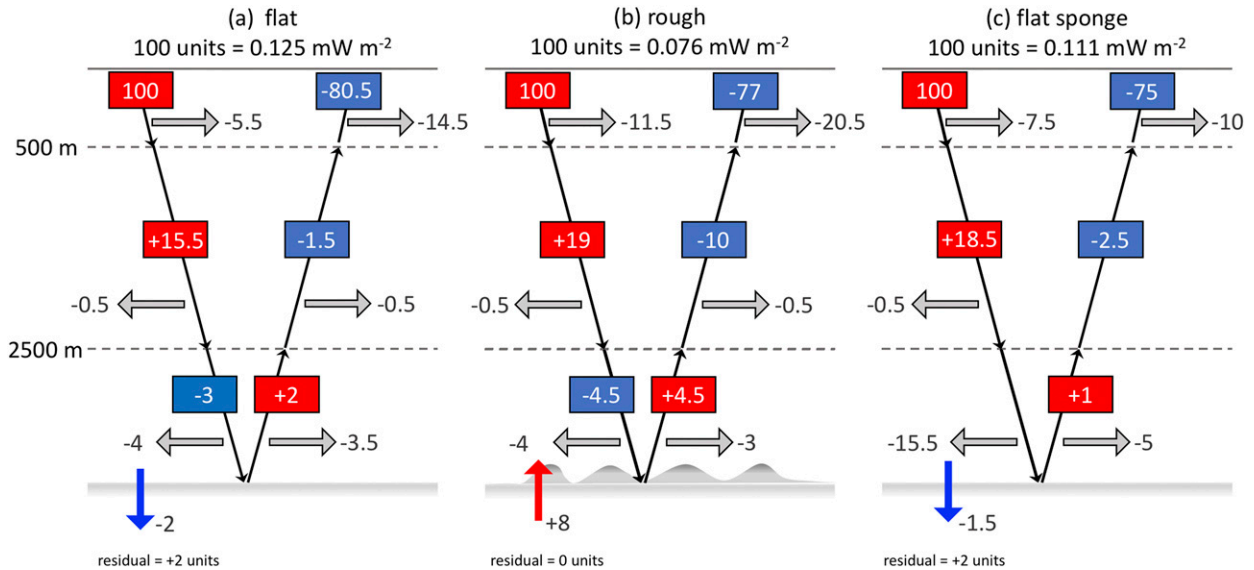
FIG. 5. Schematic life cycle showing energy sources and sinks for internal waves in each simulation: (a) flat (case A), (b) rough (case B), and (c) flat sponge (case C). The ocean depth is divided into three regions: the upper ocean (above 500 m), the deep (below 2500 m), and the interior (500–2500 m). Red boxes indicate the surface spontaneous generation or interior amplification of internal waves by the nonwave flow. All energy fluxes are normalized by setting the upper 500-m generation/amplification of downgoing waves equal to 100 units in each case. Blue boxes indicate the absorption of internal wave energy by the nonwave flow. Gray arrows indicate dissipation. Arrows through the base of the ocean indicate (a),(c) wave energy loss through bottom drag (blue arrows) or (b) wave generation/amplification in the case of rough topography (red arrow). The residual in the energy budget is indicated below each subfigure and is less than 2% in all cases.

(C) have a comparable dissipation of the downgoing energy in the surface region of order 5%–10%. In both cases, the downgoing wave field is amplified by the mean flow in the interior by 15%–20%, with minimal dissipation. Differences arise in the deep region. In case (A) with no sponge, the energy fluxes are comparable for downgoing and reflected upgoing waves, with about 4 units of dissipation for each and equal and opposite mean-to-wave terms. By contrast, case (C) with the viscous sponge exhibits very large (15 unit) dissipation of the downgoing wave energy and, therefore, negligible mean-to-wave interactions because (it would appear) the waves that would have interacted with the mean flow have instead dissipated. However, even with the sponge present, there is still substantial reflection of waves off the bottom; these waves then dissipate further as they propagate back through the sponge and out of the deep region. Of the 100 units of energy injected at the surface, case (A) retains 99 units at this point in the cycle, and case (C) retains 89.5. In both cases, the upgoing waves lose a small amount of energy back to the mean flow as they propagate through the interior, but this is an order of magnitude less than the amplification seen by the downgoing waves. The reason is that the downgoing waves are generated by shearing and straining of surface fronts and filaments and are, therefore, naturally

concentrated in regions of strong mean flows as they propagate down. As the waves reflect off the bottom, they spread out and tend to be less concentrated in these regions and, consequently, lose less energy to the mean flow because they are (on average) interacting with weaker mean currents. In case (A), 97 units of upgoing wave energy reach the surface layer, compared to 87 units in case (C). In both cases, $O(10\%)$ of this energy is dissipated in the surface region, with the remainder being reabsorbed by the mean flow.

The source and sink terms shown in Fig. 5 are individually summed in Table 1 to give an indication of the net amount of reabsorption of wave energy by the mean flow versus dissipation. Comparing cases (A) and (C), the addition of the viscous sponge has very little effect on the net magnitude of wave dissipation (see also Fig. 3). Instead, the sponge reduces the amount of wave energy being transferred to and from the mean flow (by $0.02 \, \text{mW m}^{-2}$) such that the fraction of dissipation increases (by 7%) but the net amount does not.

Let us now consider the rough bottom simulation (B) and how it differs from the flat bottom simulation without the sponge (A). The rough bottom simulation has a small, positive bottom flux of 8 units instead of the 2-unit sink of energy to bottom drag on the flat bottom. However, the net effect of the deep layer (excepting the

TABLE 1. Dissipation vs reabsorption of generated/amplified energy in the three simulations: (A) flat, (B) rough, and (C) flat sponge. The generation/amplification is the sum of all red sources (including bottom generation) in Fig. 5. MTW reabsorption is the sum of all blue boxes. Dissipation is the sum of all gray arrows.

Case	Generation/amplification	MTW reabsorption	Dissipation
(A)	117.5 units	82.5 units	28.5 units
	$0.15\,\mathrm{mW\,m^{-2}}$	$0.11\,\mathrm{mW\,m^{-2}}$	$0.04\,\mathrm{mW\,m^{-2}}$
	(100%)	(70%)	(25%)
(B)	131.5 units	91.5 units	40 units
	$0.10\,\mathrm{mW\,m^{-2}}$	$0.06\,\mathrm{mW\,m^{-2}}$	$0.03\,\mathrm{mW\,m^{-2}}$
	(100%)	(70%)	(30%)
(C)	119.5 units	77.5 units	38.5 units
	$0.13\,\mathrm{mW\,m^{-2}}$	$0.09\,\mathrm{mW\,m^{-2}}$	$0.04\,\mathrm{mW\,m^{-2}}$
	(100%)	(65%)	(32%)

bottom fluxes) in the rough bottom simulation is essentially indistinguishable from the flat bottom simulation. The rough topography acts to strengthen both the percentage amplification and decay of down- and upgoing wave energy, respectively, as a result of the larger vertical shear in the interior (e.g., Fig. 1d). However, the increase in the decay of upgoing waves in the interior is disproportionally larger. The net interior decay becomes only a factor of 2 smaller than the downgoing amplification (-10 vs $+19$ units), rather than the order of magnitude ratio (-1.5 vs $+15.5$ units) seen in the flat bottom simulation.

Collectively, the above results suggest that the effect of rough topography is (i) a reduction in the energetic asymmetry between spontaneously generated downgoing waves and their reflections and (ii) a net source of energy from the bottom interaction rather than a net

sink. However, in all three simulations, regardless of the bottom boundary, the net amount of dissipation remains around 30% and the absorption of wave energy into the mean flow about 70%, as a fraction of total generation and amplification (see Table 1).

d. Spatial distribution of energy sources and sinks

Here, we focus on the rough bottom simulation (B) to examine the spatial structure of the mean-to-wave energy fluxes and dissipation.

1) MEAN-TO-WAVE FLUXES

Figure 6 displays the net MTW conversion for (Fig. 6a) the downgoing waves and (Fig. 6b) the upgoing waves for a transect in the center of the channel at $y = 250$ km. The MTW conversion is almost entirely into the downgoing waves from the mean flow (red; greater than zero) and from upgoing waves to the mean flow (blue; less than zero), except near topography. The gray contour on the plots encloses regions where the mean flow speed exceeds $6\,\mathrm{cm\,s^{-1}}$. These regions of large mean flow are the only places where significant mean-to-wave conversions occur. The largest mean-to-wave conversions occur in the top 500 m, where the mean flows are strongest.

Figures 7a and 7b show the vertically summed MTW conversions for the upper ocean, above 500 m. Strong generation and amplification (up to $6\,\mathrm{mW\,m^{-2}}$ for a 4-day average) of downgoing waves is present in regions of strong mean flow, including fronts and the periphery of eddies. The MTW conversion is especially large along thin fronts and filaments in the south of the domain where the Rossby number (see Fig. 1b) is high, consistent with spontaneous generation, as
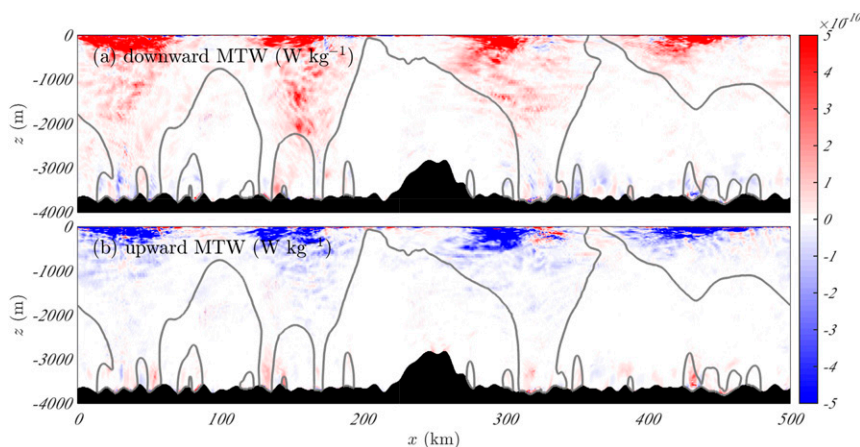

FIG. 6. The MTW energy conversion for (a) downward- and (b) upward-traveling waves at $y = 250$ km. Gray contours correspond to mean flow speeds of $6\,\mathrm{cm\,s^{-1}}$. Bottom topography along the transect is shaded in black.
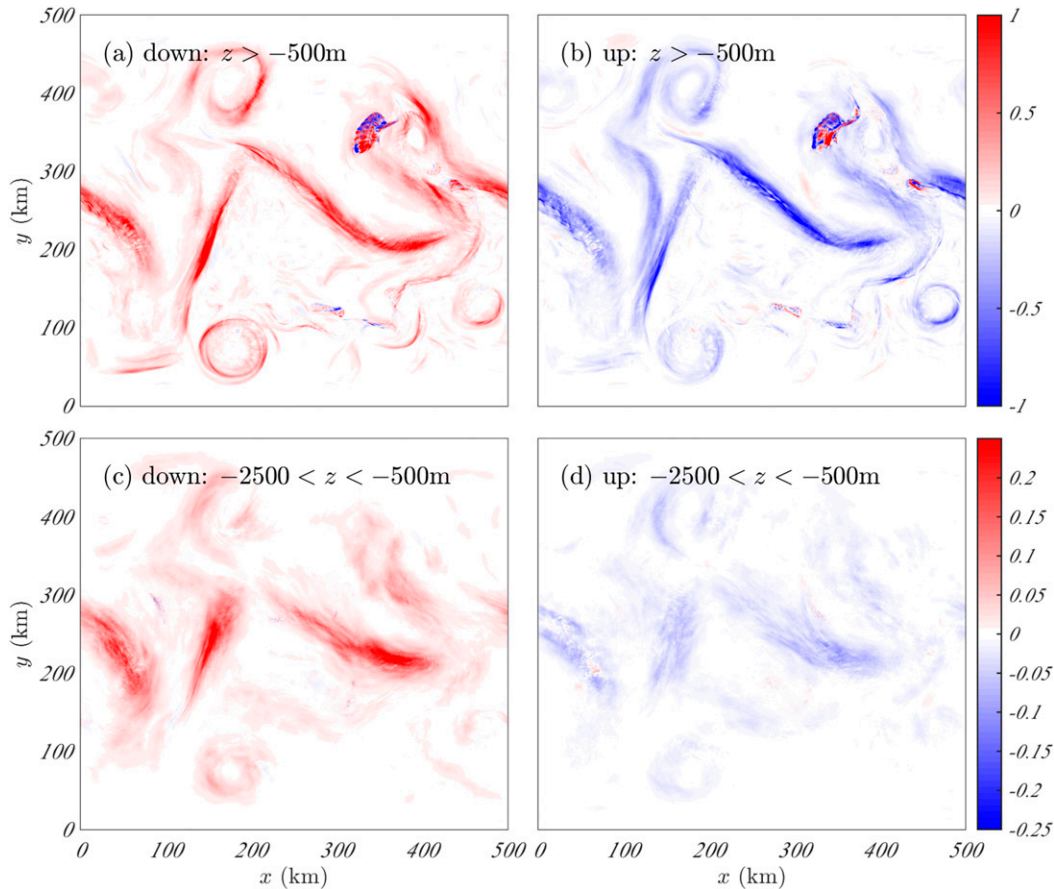
FIG. 7. The MTW energy conversion (mW m^{-2}) for (a),(c) downward- and (b),(d) upward-traveling waves integrated over the upper-ocean and interior regions for the rough bottom simulation.

described by Shakespeare and Hogg (2017a). As wave energy generated at the surface propagates downward, it disperses and interacts with the deep-reaching (geostrophic) mesoscale jets and eddies in the interior. Thus, as shown in Fig. 7c, the MTW energy conversion is smoother and broader in this interior region but is still largest directly beneath the sites of strong surface generation. The amplified downgoing waves then reflect off the rough bottom, further scattering the energy. As these reflected waves pass back through the ocean interior, they now decay where they encounter mean flows (Fig. 7d), but the prior scattering and dispersal of the energy implies that the upgoing waves, on average, encounter mean flows less often than the downgoing waves and, therefore, experience less energy exchange with the mean flow. Similarly, the reabsorption of upgoing waves into the surface mean flow (Fig. 7b), while still concentrated in the same regions, tends to be smoother and weaker than the generation and energization of downgoing waves (Fig. 7a).

Thus far, we have only considered the total MTW energy conversion for the waves. In Fig. 8, we show the downgoing MTW energy conversion for the same transect as in Fig. 6, but split into the (Fig. 8b) vertical shear/potential and (Fig. 8c) horizontal shear contributions identified in Eq. (4). Equivalent behavior is seen for the components of the upgoing MTW energy conversion (not shown). According to our earlier scaling analysis (5), the horizontal shear terms should scale with the Rossby number (Fig. 8d) and the vertical shear/potential terms with the Froude number (Fig. 8a). We observe that the vertical shear/potential terms do, indeed, scale in both sign and magnitude with the local Froude number of the mean flow, $\mathrm{Fr} = \partial_z \sqrt{\overline{u}^2 + \overline{v}^2}/N$. The small regions of negative MTW conversion in the upper 500 m in Fig. 8b can now be identified with regions where the Froude number changes sign—that is, where the vertical shear reverses (the flow speed increases with depth). The horizontal shear MTW terms are negligible, in comparison to the other MTW terms, and show no significant correlation in sign or magnitude with the local
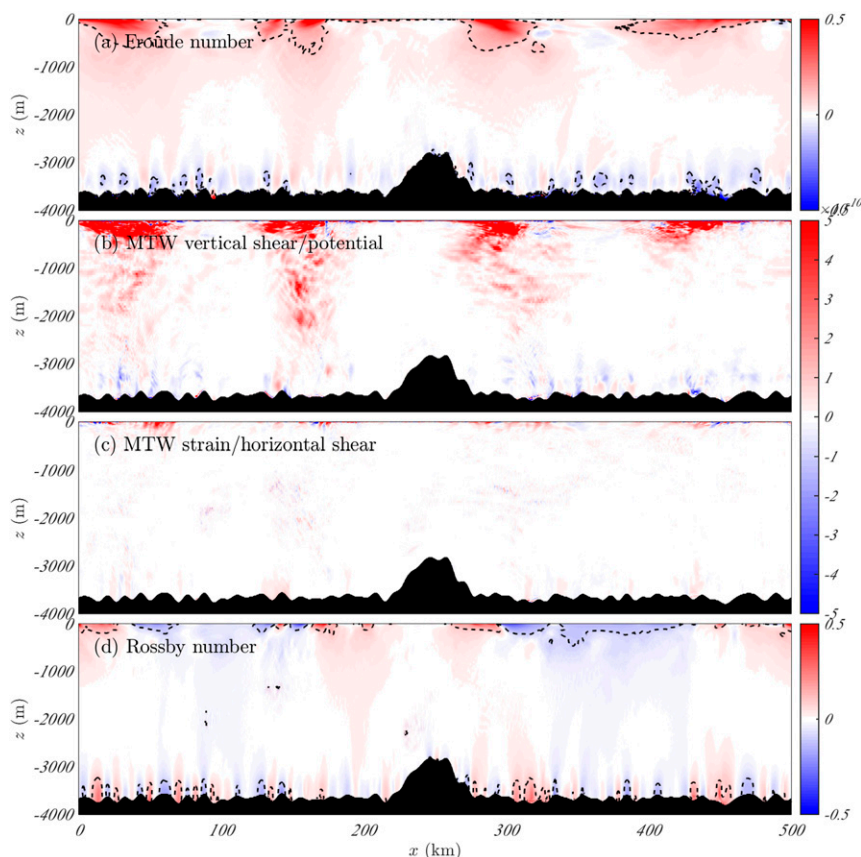
FIG. 8. The (a) Froude number $\mathrm{Fr} = \partial_z \sqrt{\overline{u}^2 + \overline{v}^2}/N$ and MTW energy conversion for down-ward-traveling waves due to the (b) vertical shear and potential terms, (c) horizontal shear terms at $y = 250$ km, and (d) Rossby number $\mathrm{Ro} = (\partial_x v - \partial_y u)/f$. The horizontal shear terms are negligible, except near the surface. As expected, the vertical shear and potential terms scale with the Froude number. The ± 0.1 contours for the Froude and Rossby numbers are indicated by dashed lines.

Rossby number, contrary to the scaling. We discuss the reasons for these differences in section 4.

2) DISSIPATION

Figure 9 displays the net wave dissipation for the (Fig. 9a) down- and (Fig. 9b) upgoing waves for the same transect as previously ($y = 250$ km). At first order, the magnitude of the dissipation is controlled by the vertical structure of the horizontal viscosity in the model, which is elevated within a few hundred meters of the boundaries (necessary for model stability; see Fig. 1c), giving rise to "bands" of elevated near-boundary dissipation in Fig. 9 for both down- and upgoing waves. However, the downgoing dissipation is also an order of magnitude larger in the regions of strong mean flow, where the internal waves are being generated and amplified, and enhanced dissipation is visible in these regions up to 1500 m above the boundary, outside the band of elevated viscosity (e.g., downgoing waves at $x = 320$ km in

Fig. 9a). The dissipation of the upgoing wave field differs from the downgoing in the interior, in that its structure is strongly influenced by the bottom topography (which affects reflections). Bands of enhanced dissipation are seen above some topographic features, for example, at $x = 30$ km in Fig. 9b. Both the down- and upgoing dissipation also show chimneylike features below the surface generation sites (cf. Fig. 8) associated with elevated wave energy in these regions.

Figure 10 shows the vertically integrated dissipation for down- and upgoing waves in the upper, interior, and deep regions defined previously. The dissipation of downgoing waves in the upper ocean is strongly concentrated along the fronts where the waves are generated. The dissipation of upgoing waves in the same upper-ocean region is weaker along these fronts but stronger in the (much larger) regions of weaker mean flow in between the fronts. Thus, the total dissipation of upgoing waves is almost double that of downgoing
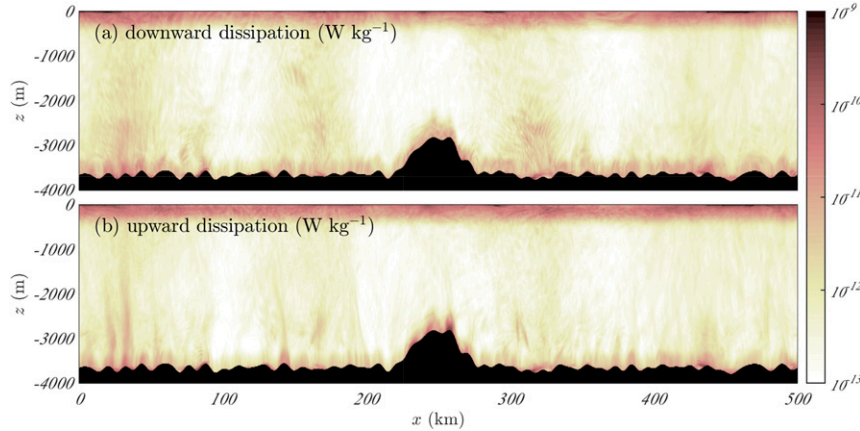
FIG. 9. The total dissipation (viscous dissipation and mixing) of (a) downward- and (b) upward-traveling waves at $y = 250$ km.

waves in this region (as per Fig. 5), despite the lower peak magnitudes. Dissipation of both down- and upgoing waves in the interior region is very weak. The dissipation of downgoing energy in this region is collocated with the energization of the waves by the mean shear (Fig. 7c), suggesting that a small amount ($\sim 3\%$) of the increase in wave energy goes directly to dissipation. In contrast to the relatively smooth downgoing dissipation, the upgoing dissipation has a clear signal from the rough topography. The dissipation in the deep region (Figs. 10e,d) is strongly influenced by topography for both the up- and downgoing wave fields.

4. Discussion

Our model results show a significant, essentially single-signed flux of mean energy into downward-propagating internal waves in regions of strong mean shear down to depths of 2500 m. Furthermore, the reflected upward-propagating waves have an opposing (but weaker) single-signed flux of wave energy back into the mean flow in the same regions. In the surface ocean above a few hundred meters' depth, the flux into downgoing waves is readily associated with spontaneous generation at sheared and strained surface density fronts and filaments (Shakespeare and Hogg 2017a). However, the amplification of downgoing waves at depth and the decay/absorption of reflected upgoing waves is a distinct process that we investigate below.

The opposite sign and collocation of the mean-to-wave conversions for the down- and reflected upgoing waves indicates that the vertical propagation direction of the wave controls the direction of energy transfer to/from the same mean flow. As shown in Fig. 8, away from boundaries, the mean-to-wave conversion (4) is entirely

dominated by the vertical shear and potential terms, and it scales with the Froude number. In these regions, the mean flow is essentially geostrophic, and the vertical mean-to-wave conversion may be reduced to a single term dependent on the mean shear by expressing the horizontal mean buoyancy gradient in terms of the shear, $\nabla_h \overline{b} = f \hat{\mathbf{z}} \times \partial_z \overline{\mathbf{u}}_h$,

$$\mathscr{F}_{\text{MTW}}^{\text{vsh}} = - \left[\left(\tilde{u}\tilde{w} - \tilde{v}\tilde{b}\frac{f}{N^2} \right) \frac{\partial \overline{u}}{\partial z} + \left(\tilde{v}\tilde{w} + \tilde{u}\tilde{b}\frac{f}{N^2} \right) \frac{\partial \overline{v}}{\partial z} \right]$$
$$= -\mathscr{F}_{\text{EP}} \cdot \frac{\partial \overline{\mathbf{u}}_h}{\partial z}, \qquad (6)$$

where $\mathscr{F}_{\text{EP}}$ is the Eliassen–Palm (EP) flux (Eliassen and Palm 1961). In the simplest case, where the shear is uniform in space and time, and the wave in question is a plane wave propagating in the x direction $\exp[i(kx + mz - \omega t)]$, it is simple to show that

$$\mathscr{F}_{\text{MTW}}^{\text{vsh}} \sim -\tilde{K}\frac{\omega^2 - f^2}{\omega^2 + f^2}\frac{k}{m}\frac{\partial \overline{u}}{\partial z}, \qquad (7)$$

where $\tilde{K} = (|\tilde{u}|^2 + |\tilde{v}|^2)/2$ is the wave kinetic energy, ω is the frequency, and k and m are the horizontal and vertical wavenumbers, respectively.[2] Thus, a wave

---

[2] Note that while (7) gives the correct sign of energy transfer for a given propagation direction, it does not account for the effect of the shear on the wave itself in modifying the frequency and vertical wavenumber. The complete solution to the problem of a wave propagating in a linear shear is discussed in Eliassen and Palm (1961), Yamanaka and Tanaka (1984), and Xie and Vanneste (2017), in varying forms. The key result is that (for small amplifications, in the absence of critical layer effects) the wave activity flux $\mathscr{F}_{\text{EP}}$ is constant, but the wave energy flux increases proportional to the change in mean flow speed (e.g., Eliassen and Palm 1961).
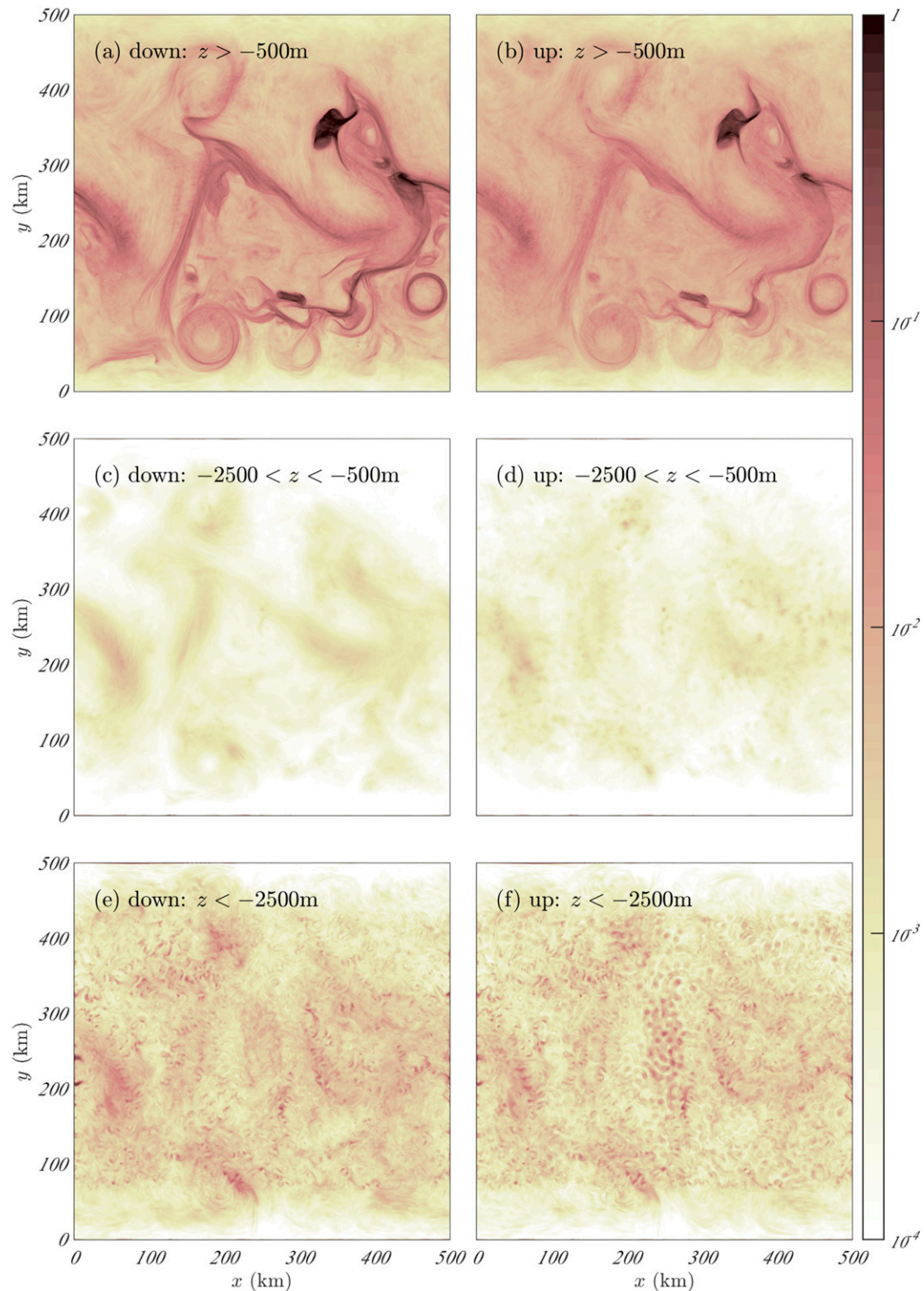
FIG. 10. The dissipation (mW m^{-2}) for (left) downward- and (right) upward-traveling waves integrated over the (top) upper-ocean, (middle) interior, and (bottom) deep regions.

propagating downward ($m < 0$) and with the shear flow ($k\partial_z\overline{u} > 0$) will amplify, whereas a wave propagating down and against the shear flow will decay. The reverse behavior occurs for a wave propagating upward ($m > 0$). The implication of this result is that waves are almost exclusively propagating with the local mean flow in the

present simulations. Specifically, waves are propagating with the flow and amplifying as they travel downward. The waves will likely still be traveling with the flow as they reflect back up, assuming that the scales of the waves are small, compared to the scale of the mean flow, such that the horizontal distance traveled is not too great and the waves remain in a similar large-scale flow environment. Thus, the waves decay as they travel upward. However, the decay of the upward waves is smaller than the amplification of the downward waves because the upward waves are less concentrated in the regions of strongest mean shear. The fact that waves are propagating with the mean flow also explains the smallness of the horizontal shear MTW terms (e.g., Fig. 8c). With the same assumptions as above (i.e., geostrophic mean flow and plane wave propagating in x), the MTW conversion associated with the horizontal shear may be written as

$$\mathscr{F}_{\text{MTW}}^{\text{hsh}} \sim \tilde{K} \frac{1}{2} \frac{\omega^2 - f^2}{\omega^2 + f^2} \frac{\partial \overline{v}}{\partial y}. \tag{8}$$

Thus, if the waves are propagating (in x) with the mean flow, we will have $\overline{v} \to 0$ and, hence, $\mathscr{F}_{\text{MTW}}^{\text{hsh}} \to 0$, as in Fig. 8c.

The mechanism of mean-to-wave energy exchange through the vertical shear is most easily understood in terms of conservation of wave action[3] $A = E/\omega$, where E is the wave energy, and ω is the Eulerian frequency (Bretherton and Garrett 1968). The mechanism is indicated in Fig. 11. An internal wave propagating in a sheared mean flow sees a Doppler-shifted Eulerian frequency of $\Omega = \omega - k\overline{u}(z)$, where k is the wavenumber in the direction of the local mean flow $\overline{u}(z)$. Thus, for a wave traveling in the direction of a decreasing mean flow, the Eulerian frequency of the wave will increase with depth/time. For action to be conserved, that wave must have a comparable increase in its energy—that is, an amplification—as seen in the simulations. In contrast, the reflection of this downgoing wave will travel upward and with the shear flow, and, thus, its frequency and energy will instead decrease with height/time. However, the fact that this upgoing decay is weaker than the downgoing amplification (e.g., Fig. 5; despite comparable energy fluxes) indicates that the upgoing waves are, on average, encountering weaker shear, especially in the flat-bottomed simulations.

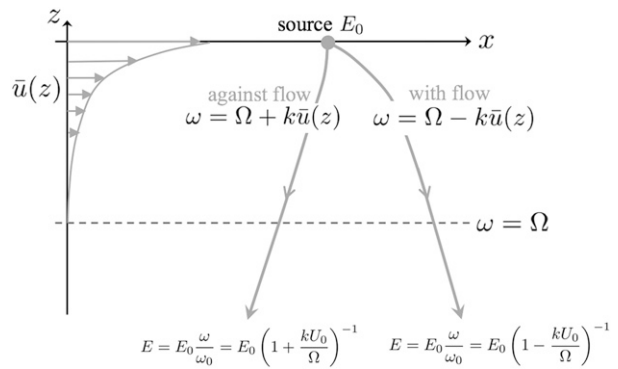As noted above, the largely uniform amplification of downgoing waves implies that they are almost

___

[3] The authors would like to acknowledge G. Wagner for pointing this out.

FIG. 11. Schematic of the amplification (decay) of wave energy in a mean shear flow $\overline{u}(z)$ for waves propagating with (against) the flow, following Eliassen and Palm (1961); Yamanaka and Tanaka (1984); and Xie and Vanneste (2017), among others. The basic principle is that wave action $A = E/\omega$, where E is the energy and ω the Eulerian frequency, is conserved so that wave energy scales with frequency. Parameter Ω is the Lagrangian (intrinsic) frequency of the wave, and $U_0 = \overline{u}(0)$ is the change in velocity seen by the wave. For small amplifications (e.g., 10%–20%, as seen in the present simulations), the fractional increase in energy is just kU_0/Ω.

exclusively propagating with the local mean flow in the present simulations. The absence of any decay of downgoing waves means that spontaneous generation must be acting to only generate waves in the direction of the local mean flow. Our conclusion is that spontaneous wave generation in other orientations is suppressed by the presence of mean shear, and, consequently, such waves are not observed in the simulations. This behavior appears to be a feature associated with spontaneous generation: the flow tends to spontaneously generate wave energy in an orientation whereby waves are locally amplified by vertical shear. We hypothesize that spontaneously generated waves are unique in this respect and that externally forced waves (e.g., via winds or tides) would behave differently, in that waves in both directions would be observed, but with one direction amplified and the other decayed. Indeed, simulations involving wind-forced internal waves (Barkan et al. 2017; Taylor and Straub 2016) show sizeable energy exchange through the horizontal shear MTW terms (which are negligible in our simulations), implying that [per Eq. (8)] such forced waves are not uniformly propagating with the local flow. However, the strongest mean-to-wave energy fluxes in those studies occur over a comparable depth range of 0–500 m, and the waves also extract energy (on average) from the mean flow. These previous studies, thus, support our hypothesis as to the uniqueness of spontaneous generation in terms of the close connection between wave propagation direction and mean shear.

5. Conclusions

Our results suggest that internal waves are spontaneously generated in locations and with appropriate scales and orientations, such that they draw net energy from the mean shear throughout the upper and interior ocean as they propagate downward. The Froude number, rather than the Rossby number, is the nondimensional parameter governing the strength of the interaction of these waves with the mean flow [i.e., Eq. (5)]. Thus, spontaneously generated internal waves may play a unique role in the ocean wave energy budget and potentially have a large source of energy available to them. Total spontaneous generation and amplification in our simulations is of order $0.1\,\mathrm{mW\,m^{-2}}$ averaged over the entire model domain, but further study is necessary to determine how these magnitudes will change with higher model resolution and scale to the real world. Theories of spontaneous generation (Shakespeare and Taylor 2016, 2014) predict an exponential increase in wave generation as fronts and filaments (which are limited by model resolution and viscous parameters) approach smaller scales. Furthermore, observations (e.g., Shcherbina et al. 2013) indicate that parameter regime of the ocean may be more extreme than that modeled here and, hence, has the potential for stronger frontogenesis and spontaneous generation. For instance, Shcherbina et al. (2013) report a mean strain rate[4] of $0.8f$ versus a mean value of $0.14f$ in the present (rough bottomed) simulation.

The internal waves in our simulations propagate over the full depth of the model and reflect off the bottom. In all our simulations, approximately 70% of the wave energy is returned to the mean flow upon reflection, mostly in the upper 500 m, with the remainder dissipated by either the downgoing or reflected upgoing waves. Thus, our simulations show that internal waves can continually exchange energy with the mean flow. This behavior is contrary to the current paradigm that internal waves predominately flux energy downscale toward dissipation. Instead, here, the waves predominately flux energy upscale, back to the (largely balanced) jets and eddies of the mean flow.

As a result, it appears that spontaneously generated waves, in isolation, are a relatively inefficient means of energy dissipation and, hence, of driving ocean mixing. However, the tendency of the waves to propagate through the ocean depth and interact with the ocean bottom suggests that in the presence of an additional bottom source of internal waves, such as small-scale internal tides or lee waves, the wave fields could interact to trigger or enhance deep-ocean mixing. These questions remain a topic for future research.

APPENDIX

Quantifying Errors Associated with the Lagrangian Filtering Method

As described in Shakespeare and Hogg (2017a), the Lagrangian filtering method involves the following steps:

1) Particle tracking. Initialize one Lagrangian particle at every model grid point and compute the path of these particles over the (1 week) analysis period. Only horizontal velocities are used for particle advection; vertical motion may be neglected (Shakespeare and Hogg 2017a).
2) Forward interpolation. At each time, (linearly) interpolate fields of interest (e.g., u, v, w, and p) from the model grid to the particle locations at that time.
3) Filtering. Perform frequency filtering for each particle.
4) Reverse interpolation. At each time, interpolate the filtered fields from the scattered particle locations back to the model grid. We use the MATLAB scatteredInterpolant() function with linear interpolation to perform this step.
5) Analysis. Compute required energy fluxes.

As time progresses, the particle locations as computed in step (1) become more concentrated in some regions (increasing resolution) and less concentrated (decreasing resolution) in others. The inhomogeneity of particles is greater for larger variations in flow speed (e.g., near the surface) and at later times. Sampling errors in the above procedure are potentially introduced in step (4) due to the degrading of the effective resolution in certain locations. To quantify these errors, we consider the case with the most inhomogeneous particle distribution: the surface layer at the end of the 1-week analysis period.

As an example, we consider the flow speed $U = \sqrt{u^2 + v^2}$ at this time, as pictured in Fig. A1

---

[4] Defined as $s = [(\partial_x u - \partial_y v)^2 + (\partial_x u + \partial_y v)^2]^{1/2}$.
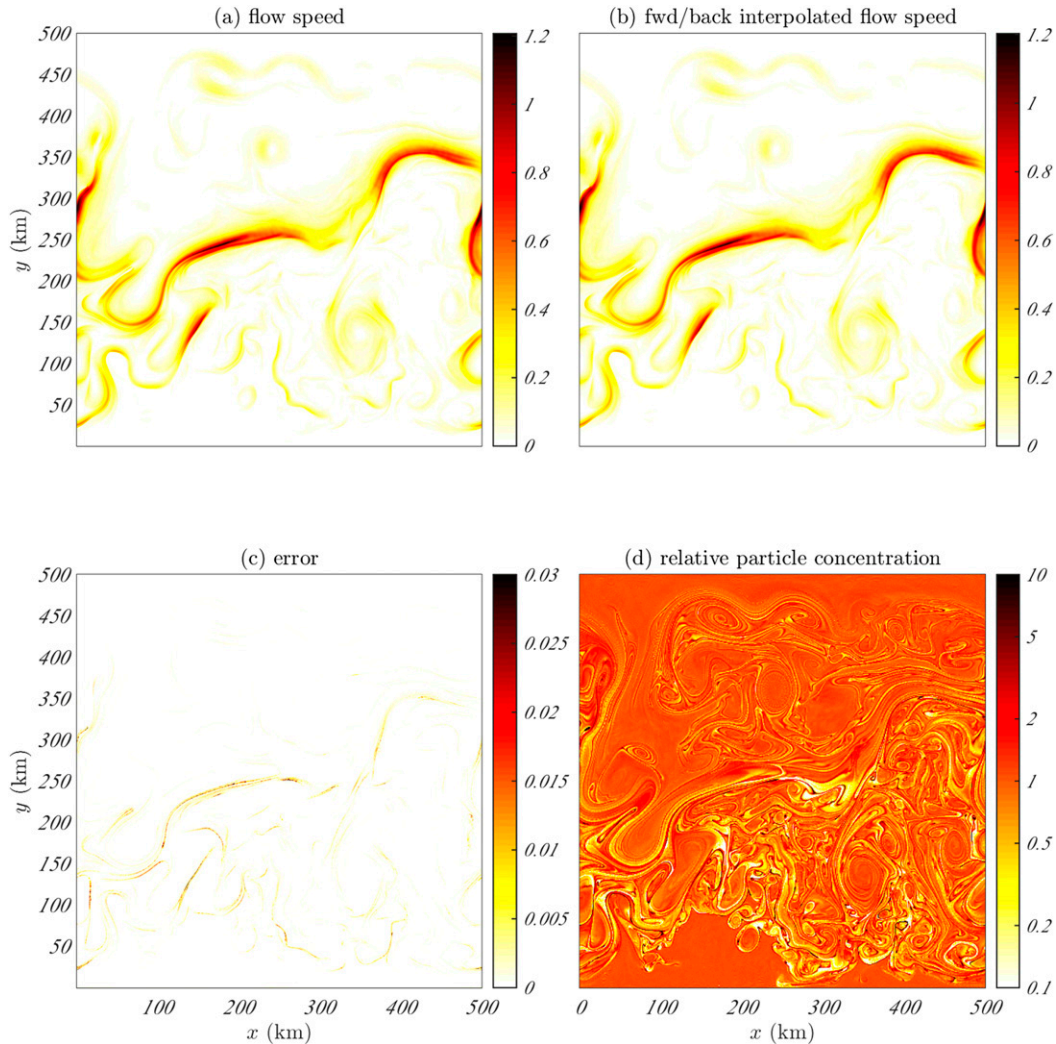
FIG. A1. Evaluation of Lagrangian forward and reverse interpolation. (a) The surface flow speed ($m\,s^{-1}$) from the model 1 week into the analysis period. (b) The flow speed (linearly) interpolated to Lagrangian particles then reverse interpolated from the scattered points back to the model grid. (c) The difference between (a) and (b). (d) The Lagrangian particle concentration at this time, relative to the initial uniform concentration.

[from the flat topography simulation (A)]. We interpolate the flow speed to the Lagrangian parcel locations at this time as per (2), then, without filtering, reverse interpolate back to the model grid as per (4). The resulting forward-/reverse-interpolated flow speed U^* is shown in Fig. A1b and is (by eye) indistinguishable from the original. The difference between the original and interpolated fields $U - U^*$ is shown in Fig. A1c and quantifies the error associated with the Lagrangian method. The errors are largest along the strong surface jets, with magnitudes of a few percent (1 to $3\,cm\,s^{-1}$). The domain mean error is mean$|U^* - U|/$mean$(U) = 0.004$, or 0.4%, which gives an estimate of the error in horizontally averaged quantities, such as domain-averaged energy fluxes. This error is negligible.

The Lagrangian particle concentration after 1 week is plotted in Fig. A1d, relative to the initial concentration (at time zero, the concentration is 1 everywhere). The relative concentration C is computed by counting the number of particles in each $1\,km \times 1\,km$ box and dividing by the original number of parcels in the region (25, or one parcel per $200\,m \times 200\,m$ grid cell). The effective resolution for a given particle concentration is $r = 200/\sqrt{C}$. It is interesting to note that the regions with the lowest particle concentrations (white regions in Fig. A1d) do not necessarily correspond to the regions with the largest errors (Fig. A1c). Instead, low concentration seems common in largely quiescent regions near the ends of jets (e.g., $x = y = 175\,km$). The cumulative density function of particle concentration is also shown
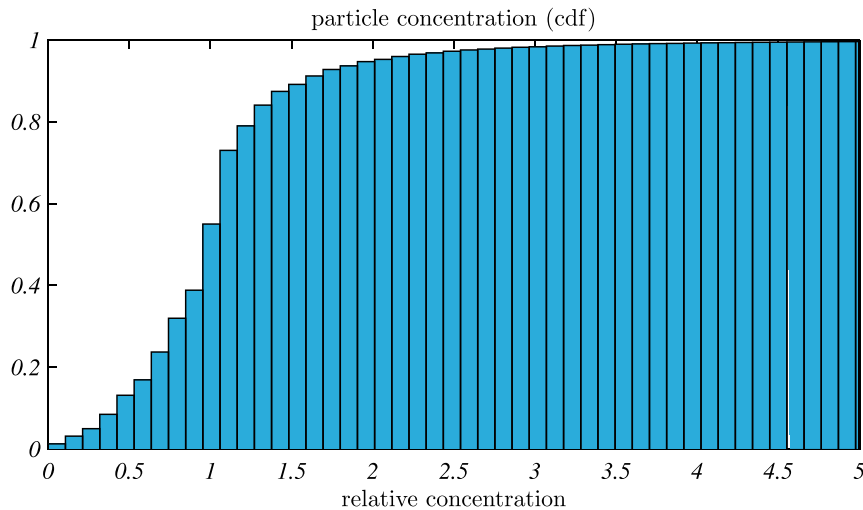
F<small>IG</small>. A2. Cumulative density function of Lagrangian particle concentration at the end of the 1-week analysis period (as shown in Fig. A1d). Concentrations are expressed relative to the initial concentration of one parcel per 200 m × 200 m grid cell. A relative concentration of 0.1 corresponds to an effective resolution of $200/\sqrt{0.1} = 632$ m; 99% of the domain has a resolution of this value or better.

in Fig. A2 and indicates that 99% of the domain has a particle concentration of greater than 0.1 (or, equivalently, an effective resolution of better than 632 m).

The above results demonstrate that the Lagrangian filtering method is robust over the time scales of interest and not subject to significant sampling error.

REFERENCES

Barkan, R., K. B. Winters, and J. C. McWilliams, 2017: Stimulated imbalance and the enhancement of eddy kinetic energy dissipation by internal waves. *J. Phys. Oceanogr.*, **47**, 181–198, https://doi.org/10.1175/JPO-D-16-0117.1.

Bell, T., 1975: Topographically generated internal waves in the open ocean. *J. Geophys. Res.*, **80**, 320–327, https://doi.org/10.1029/JC080i003p00320.

Bretherton, F. P., and C. J. R. Garrett, 1968: Wave trains in inhomogeneous moving media. *Proc. Roy. Soc. London*, **302A**, 529–554, https://doi.org/10.1098/rspa.1968.0034.

Eliassen, A., and E. Palm, 1961: On the transfer of energy in stationary mountain waves. *Geofys. Publ.*, **22** (3), 1–23.

Grisouard, N., M. B. Fox, and J. Nijjer, 2016: Radiation of internal waves by symmetrically unstable fronts. *Eighth Int. Symp. on Stratified Flows*, San Diego, CA, International Association for Hydro-Environment Engineering and Research, 8 pp.

Jones, W. L., 1967: Propagation of internal gravity waves in fluids with shear flow and rotation. *J. Fluid Mech.*, **30**, 439–448, https://doi.org/10.1017/S0022112067001521.

Marshall, J., A. Adcroft, C. Hill, L. Perelman, and C. Heisey, 1997: A finite-volume, incompressible Navier Stokes model for studies of the ocean on parallel computers. *J. Geophys. Res.*, **102**, 5753–5766, https://doi.org/10.1029/96JC02775.

Müller, P., G. Holloway, F. Henyey, and N. Pomphrey, 1986: Nonlinear interactions among internal gravity waves. *Rev. Geophys.*, **24**, 493–536, https://doi.org/10.1029/RG024i003p00493.

Munk, W., 1981: Internal waves and small-scale processes. *Evolution of Physical Oceanography*, B. Warren and C. Wunsch, Eds., 264–291.

Nagai, T., A. Tandon, E. Kunze, and A. Mahadevan, 2015: Spontaneous generation of near-inertial waves by the Kuroshio Front. *J. Phys. Oceanogr.*, **45**, 2381–2406, https://doi.org/10.1175/JPO-D-14-0086.1.

Nikurashin, M., and R. Ferrari, 2011: Global energy conversion rate from geostrophic flows into internal lee waves in the deep ocean. *Geophys. Res. Lett.*, **38**, L08610, https://doi.org/10.1029/2011GL046576.

Plougonven, R. and V. Zeitlin, 2009: Nonlinear development of inertial instability in a barotropic shear. *Phys. Fluids*, **21**, 106601, https://doi.org/10.1063/1.3242283.

Polzin, K. L., and Y. V. Lvov, 2011: Toward regional characterizations of the oceanic internal wavefield. *Rev. Geophys.*, **49**, RG4003, https://doi.org/10.1029/2010RG000329.

Ribstein, B., R. Plougonven, and V. Zeitlin, 2014: Inertial versus baroclinic instability of the Bickley jet in continuously stratified rotating fluid. *J. Fluid Mech.*, **743**, 1–31, https://doi.org/10.1017/jfm.2014.26.

Shakespeare, C. J., and J. R. Taylor, 2014: The spontaneous generation of inertia–gravity waves during frontogenesis forced by large strain: Theory. *J. Fluid Mech.*, **757**, 817–853, https://doi.org/10.1017/jfm.2014.514.

——, and ——, 2016: Spontaneous wave generation at strongly strained density fronts. *J. Phys. Oceanogr.*, **46**, 2063–2081, https://doi.org/10.1175/JPO-D-15-0043.1.

——, and A. M. Hogg, 2017a: Spontaneous surface generation and interior amplification of internal waves in a regional-scale ocean model. *J. Phys. Oceanogr.*, **47**, 811–826, https://doi.org/10.1175/JPO-D-16-0188.1.

——, and ——, 2017b: The viscous lee wave problem and its implications for ocean modelling. *Ocean Modell.*, **113**, 22–29, https://doi.org/10.1016/j.ocemod.2017.03.006.

Shcherbina, A. Y., E. A. D'Asaro, C. M. Lee, J. M. Klymak, M. J. Molemaker, and J. C. McWilliams, 2013: Statistics of vertical

vorticity, divergence, and strain in a developed submesoscale turbulence field. *Geophys. Res. Lett.*, **40**, 4706–4711, https://doi.org/10.1002/grl.50919.

Taylor, S., and D. Straub, 2016: Forced near-inertial motion and dissipation of low-frequency kinetic energy in a wind-driven channel flow. *J. Phys. Oceanogr.*, **46**, 79–93, https://doi.org/10.1175/JPO-D-15-0060.1.

Wunsch, C., and R. Ferrari, 2004: Vertical mixing, energy, and the general circulation of the oceans. *Annu. Rev. Fluid Mech.*, **36**, 281–314, https://doi.org/10.1146/annurev.fluid.36.050802.122121.

Xie, J.-H., and J. Vanneste, 2017: Interaction between mountain waves and shear flow in an inertial layer. *J. Fluid Mech.*, **816**, 352–380, https://doi.org/10.1017/jfm.2017.39.

Yamanaka, M. D., and H. Tanaka, 1984: Propagation and breakdown of internal inertio-gravity waves near critical levels in the middle atmosphere. *J. Meteor. Soc. Japan*, **62**, 1–17, https://doi.org/10.2151/jmsj1965.62.1_1.